

Fronthaul-Efficient Distributed Cooperative 3D Positioning with Quantized Latent CSI Embeddings

Tong An, Jiwei Zhao, Jiayang Shi, Bin Zheng, Kai Yu, Maged Elkashlan,
George K. Karagiannidis, *Fellow, IEEE*, Hongsheng Chen, *Fellow, IEEE*

Abstract—High-precision three-dimensional (3D) positioning in dense urban non-line-of-sight (NLOS) environments benefits significantly from cooperation among multiple distributed base stations (BSs). However, forwarding raw CSI from multiple BSs to a central unit (CU) incurs prohibitive fronthaul overhead, which limits scalable cooperative positioning in practice. This paper proposes a learning-based edge-cloud cooperative positioning framework under limited-capacity fronthaul constraints. In the proposed architecture, a neural network is deployed at each BS to compress the locally estimated CSI into a quantized representation subject to a fixed fronthaul payload. The quantized CSI is transmitted to the CU, which performs cooperative 3D positioning by jointly processing the compressed CSI received from multiple BSs. The proposed framework adopts a two-stage training strategy consisting of self-supervised local training at the BSs and end-to-end joint training for positioning at the CU. Simulation results based on a 3.5 GHz 5G NR compliant urban ray-tracing scenario with six BSs and 20 MHz bandwidth show that the proposed method achieves a mean 3D positioning error of 0.48 m and a 90th-percentile error of 0.83 m, while reducing the fronthaul payload to 6.25% of lossless CSI forwarding. The achieved performance is close to that of cooperative positioning with full CSI exchange.

Index Terms—Cooperative positioning, CSI, embedded fronthaul, edge-cloud cooperative processing, multi-BS fusion, deep learning.

I. INTRODUCTION

NEXT-generation cellular systems are evolving from connectivity-centric infrastructures into cloud-native platforms that natively support communication, sensing, and high-precision three-dimensional (3D) positioning [1]–[6]. Positioning is increasingly treated as a built-in network service to enable location-aware applications such as intelligent transportation, extended reality, and low-altitude aerial mobility [1],

This work was supported by the National Natural Science Foundation of China (62071423, U25A20520), the Natural Science Foundation of Zhejiang Province under Grant (LR23F010004), the Top-Notch Young Talent of Zhejiang Province, Fundamental Research Funds for the Central Universities (226-2024-00125), the Postdoctoral Fellowship Program of CPSF under Grant (GZC20241521), the Postdoctoral Science Preferential Funding of Zhejiang Province (ZJ2024054), the China Postdoctoral Science Foundation Funded Project (2024M762827, 2025T180960), and the Key Research and Development Program of Zhejiang Province under Grant No. 2024C01160. (Corresponding author: Jiwei Zhao.)

Tong An, Jiwei Zhao, Jiayang Shi, Bin Zheng and Hongsheng Chen are with the College of Information Science & Electronic Engineering, Zhejiang University, Hangzhou, China (e-mail: {antoon, jackokie, jiayangshi, zhengbin, hansomchen}@zju.edu.cn). Kai Yu is with the KTH Royal Institute of Technology, Stockholm, Sweden (e-mail: kayu@kth.se). Maged Elkashlan is with the School of Electronic Engineering and Computer Science, Queen Mary University of London, London, UK (e-mail: maged.elkashlan@qmul.ac.uk). George K. Karagiannidis is with the Department of Electrical and Computer Engineering, Aristotle University of Thessaloniki, Thessaloniki, Greece (e-mail: geokarag@auth.gr).

[2]. In dense urban scenarios such as street-level deployments, however, Global Navigation Satellite Systems (GNSS) often become unreliable due to blockage and severe multipath, motivating terrestrial positioning solutions that exploit ubiquitous cellular infrastructure under non-line-of-sight (NLOS) propagation conditions [7]–[9]. At the same time, cloud-native and cooperative radio access network (RAN) architectures, including fully or partially decoupled reception and cell-free networks, have made centralized multi-point processing increasingly feasible [4], [6], [7]. While such architectures provide a natural foundation for cooperative positioning across multiple distributed base stations, their practical deployment is fundamentally constrained by the need to aggregate high-dimensional channel state information (CSI) over fronthaul links with limited capacity, latency, and scalability.

A. Positioning with CSI Fingerprinting

In modern multiple-input multiple-output orthogonal frequency division multiplexing (MIMO-OFDM) systems, CSI captures rich, location-dependent multipath signatures that serve as high-dimensional radio fingerprints [2]. These signatures are characterized by the spatial diversity provided by antenna arrays and by delay-induced phase variations across frequency-domain subcarriers, which together enable informative 3D localization. This characteristic is particularly relevant in complex propagation environments where reflections and scattering dominate and can be accurately modeled and measured [3]. Existing CSI-based positioning approaches can be broadly categorized into model-based and learning-based methods. Model-based techniques estimate geometric parameters such as angle-of-arrival and time-related quantities, including time-of-flight and time-difference-of-arrival, using subspace methods and statistical inference [10]–[17]. These methods are interpretable and effective when dominant propagation components can be reliably identified. However, in dense urban NLOS scenarios, the strongest received path often corresponds to a reflected or scattered component rather than a direct path, which can significantly degrade the robustness of purely geometry-driven localization. Learning-based CSI fingerprinting provides an alternative by directly learning a mapping from CSI observations to spatial coordinates without explicitly estimating intermediate propagation parameters. Early work explored CSI phase fingerprints and convolutional neural network architectures [18], [19], while more recent studies have incorporated attention mechanisms and residual designs to better exploit the structure of massive-MIMO CSI [20]–[24]. Related learning-based formulations have also been

investigated for passive probabilistic fingerprinting and tracking [25]–[28], sparse Bayesian learning for MIMO–OFDM localization [29], and integrated sensing and communications scenarios [30], [31]. Despite their demonstrated potential, learning-based fingerprinting approaches face practical challenges in data acquisition, environmental dynamics, and generalization. These challenges become more pronounced as CSI dimensionality increases with bandwidth, antenna count, and deployment scale [32].

B. Cooperative Positioning with Multiple BSs

A key limitation of CSI fingerprinting based on a single base station (BS) lies in its restricted spatial perspective [2]. In dense urban non-line-of-sight (NLOS) environments, different user locations may produce highly similar CSI observations at an individual BS due to common blockage patterns, dominant reflections, and limited angular diversity, which introduces uncertainty in the mapping from CSI to position [33]. This uncertainty cannot be fully resolved by increasing bandwidth or antenna count at a single site, as the underlying propagation geometry remains partially unobservable from a single viewpoint [1]. Cooperative positioning across multiple distributed BSs provides a systematic way to alleviate this limitation by exploiting complementary propagation perspectives and macro-diversity [34]–[36]. By jointly processing CSI measurements collected at spatially separated BSs, the receiver gains access to multiple independent views of the same environment, which improves the identifiability and robustness of location inference. Prior studies have shown that multi-BS cooperation can substantially enhance localization accuracy in challenging NLOS scenarios, including probabilistic fusion of multi-point CSI and learning-based cooperative positioning frameworks [34], [37]. Related cooperative localization concepts have also been investigated in other distributed sensing systems, such as wireless sensor networks and distributed MIMO radar-like architectures [35], [36]. While multi-BS cooperation offers clear accuracy advantages, its practical realization is constrained by the need to aggregate CSI from multiple BSs at a central unit. Forwarding raw high-dimensional CSI from each BS incurs prohibitive fronthaul overhead, which scales linearly with the number of cooperating BSs, antennas, and subcarriers. As a result, the scalability of cooperative positioning is largely determined by how CSI is represented and conveyed over fronthaul links with limited capacity.

C. Cooperative Positioning under Fronthaul Constraints

In cooperative positioning, CSI from multiple distributed BSs must be aggregated at a central unit to enable joint processing. This aggregation relies on fronthaul links that are subject to limited capacity and latency constraints in practical cloud-native radio access networks [1]. The fronthaul payload associated with CSI aggregation scales linearly with the number of antennas, subcarriers, time samples, and cooperating BSs [38]. To reduce fronthaul overhead, CSI compression prior to transmission is commonly considered. Most existing CSI compression and feedback techniques developed for massive MIMO systems are reconstruction-oriented, with the

objective of accurately recovering CSI at the receiver for tasks such as beamforming and link adaptation [39]–[41]. Representative approaches include compressive sensing-based feedback schemes [41]–[43], adaptive compression strategies [44], learning-based CSI feedback frameworks [40], and subsequent advances such as changeable-rate designs and quantization-aware modules [45], [46], as well as learning-to-optimize formulations that reduce complexity while maintaining reconstruction quality [47]. For cooperative positioning, however, the objectives and constraints differ from those of communication-centric CSI acquisition. Accurate reconstruction of CSI is not necessarily aligned with minimizing localization error under a strict fronthaul bit budget, particularly in NLOS environments where only specific spatial or delay-related structures may be informative for distinguishing user locations [1]. Moreover, even when compact representations are extracted at each BS, the resulting features are often continuous and stored in floating-point formats, which can still impose substantial fronthaul overhead when multiple BSs participate in cooperative positioning [42]–[44]. These observations indicate that the scalability of cooperative positioning under fronthaul constraints is largely determined by how CSI is represented and conveyed to the central unit. This, in turn, motivates the consideration of task-oriented CSI representations that explicitly account for fronthaul constraints and support joint processing across multiple BSs for localization.

D. Our Framework and Contributions

This work considers fronthaul-constrained cooperative 3D positioning and develops a distributed edge-cloud framework for joint localization across multiple BSs. In the proposed architecture, each BS processes its locally estimated CSI into a compact representation and transmits a quantized version to a central unit for cooperative positioning. The central unit jointly infers the user position from the quantized CSI received from multiple BSs, without reconstructing the original CSI. To train the proposed framework, we adopt a two-stage training strategy consisting of local training and joint training. The local training stage is deployed at each BS and focuses on stabilizing CSI representations through self-supervised learning. The joint training stage is performed between the BSs and the central unit, optimizing the entire cooperative positioning pipeline under fronthaul quantization constraints. By setting the latent presentation dimension and quantization resolution at each BS, the proposed framework explicitly controls the fronthaul payload for scalable multi-BS cooperation.

The main contributions of this work are summarized as follows:

- **Edge-cloud cooperative 3D positioning under fronthaul constraints:** We develop a distributed edge-cloud cooperative positioning framework consisting of a local processing stage at each BS and a central inference stage. In this framework, each BS maps its locally estimated CSI into a fixed-length latent representation and transmits a uniformly quantized version under an explicit fronthaul bit budget. The central unit jointly infers the 3D user position from the quantized CSI representations received from

multiple BSs. This formulation enables scalable multi-BS cooperation without forwarding raw high-dimensional CSI.

- **Multi-BS fusion with structured frequency-domain inference:** We design a central inference mechanism that performs cooperative 3D positioning directly from quantized CSI representations. The mechanism integrates side-information-assisted fusion to weight contributions from different BSs, suppressing NLOS interference from severely attenuated links. Combining spatial and frequency-domain processing, the mechanism leverages structured frequency-domain information to enhance robustness and identifiability in NLOS environments. This design effectively exploits the rich multipath signatures encoded in wideband MIMO-OFDM CSI for positioning.
- **Two-stage training for distributed sensing and centralized inference:** We develop a two-stage training strategy consisting of local training and joint training. The local training at each BS is based on unquantized CSI and conducted in a self-supervised manner to stabilize latent CSI representations. The joint training at the central unit is based on compressed-then-quantized CSI presentation from multi-BSs and optimizes the entire cooperating positioning pipeline through end-to-end learning. The proposed framework is evaluated in a 3.5 GHz 5G NR-compliant urban ray-tracing scenario with six BSs, demonstrating sub-meter 3D positioning accuracy with a fronthaul payload reduced to 6.25% of lossless CSI forwarding.

The rest of the paper is organized as follows. Section II introduces the system model and the fronthaul-limited formulation. Section III presents the proposed edge-cloud cooperative positioning architecture and the quantization-aware training procedure. Section IV provides the simulation setup and performance evaluation. Section V concludes the paper and discusses future research directions.

Notations: In this paper, $(\cdot)^{-1}$, $(\cdot)^*$, $(\cdot)^H$, and $(\cdot)^T$ denote the inverse, complex conjugate, conjugate transpose, and transpose, respectively. \mathbf{I}_N denotes the $N \times N$ identity matrix. $\|\cdot\|_2$ and $\|\cdot\|_F$ denote the Euclidean norm (for vectors) and the Frobenius norm (for matrices), respectively. $\text{diag}(\cdot)$ constructs a diagonal matrix and $\text{vec}(\cdot)$ stacks all entries of a matrix into a column vector. $\Re\{\cdot\}$, $\Im\{\cdot\}$, and $\angle(\cdot)$ denote the real part, imaginary part, and complex argument, respectively. For a bitstream $\mathbf{b} \in \{0, 1\}^B$, $\text{len}(\mathbf{b}) = B$ denotes its length in bits.

II. SYSTEM MODEL AND FRAMEWORK OVERVIEW

In this section, we introduce the system and channel model for uplink CSI acquisition at distributed BSs, followed by an overview of the proposed edge-cloud cooperative positioning framework under fronthaul constraints.

A. System and Channel Model

As illustrated in Fig. 1, we consider a Cloud-RAN (C-RAN) architecture within urban scenario, where L distributed base

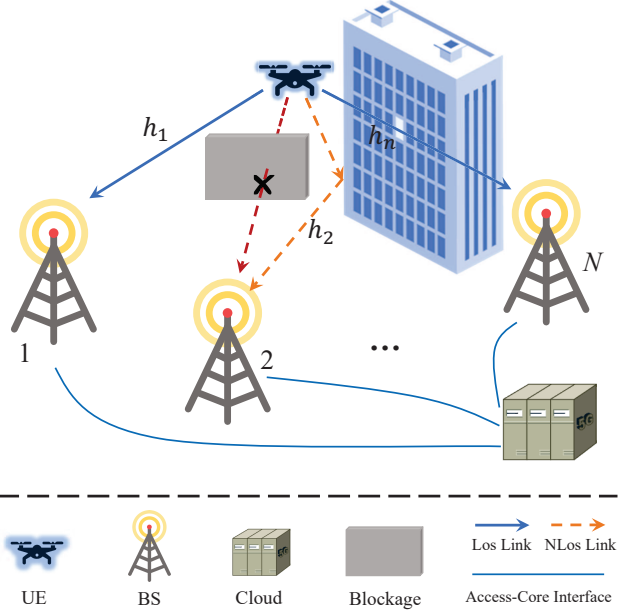


Fig. 1: Cloud-RAN architecture for cooperative 3D positioning in urban NLOS environments.

stations (BSs) are connected to a centralized cloud unit (CU) via fronthaul links. Each BS is equipped with N_r receive antennas and operates an OFDM system with N_{sc} subcarriers. To capture temporal variability, the UE transmits pilot signals over T time slots, yielding a sequence of pilot observations at each BS and a corresponding CSI estimate in each slot. The UE position $\mathbf{p} \in \mathbb{R}^3$ is assumed to remain quasi-static over a positioning snapshot of T slots, which is reasonable when T lies within a short channel coherence interval.

Let the known 3D position of BS l be $\mathbf{s}^{(l)} \in \mathbb{R}^3$, and let the UE position be $\mathbf{p} \in \mathbb{R}^3$. The wideband MIMO-OFDM channel between the UE and BS l depends on \mathbf{p} through propagation geometry and environment-specific scattering. A generic representation for the frequency-domain channel vector on subcarrier n at time slot t is

$$\mathbf{h}_{t,n}^{(l)}(\mathbf{p}) = \sum_{k=1}^{K_l} \alpha_{t,k}^{(l)} \mathbf{a}_r^{(l)}(\vartheta_{t,k}^{(l)}, \varphi_{t,k}^{(l)}) e^{-j2\pi f_n \tau_{t,k}^{(l)}(\mathbf{p})}, \quad (1)$$

where K_l is the number of effective paths (including reflected/scattered components), $\alpha_{t,k}^{(l)} \in \mathbb{C}$ is the complex gain of path k , $\mathbf{a}_r^{(l)}(\cdot) \in \mathbb{C}^{N_r}$ is the BS receive-array response parameterized by azimuth/elevation angles (ϑ, φ) , and $\tau_{t,k}^{(l)}(\mathbf{p})$ is the propagation delay of path k .

Within one positioning snapshot, \mathbf{p} is assumed constant, while the channel may still exhibit residual slot-to-slot variations due to small-scale fading, dynamic blockage, or receiver impairments; accordingly, we retain the time index t . When geometry-related parameters are effectively constant over the snapshot, the t -dependence of $\tau_{t,k}^{(l)}$ and $(\vartheta_{t,k}^{(l)}, \varphi_{t,k}^{(l)})$ can be dropped as a special case. Stacking $\{\mathbf{h}_{t,n}^{(l)}\}_{n=1}^{N_{sc}}$ yields the CSI matrix $\mathbf{H}_t^{(l)}(\mathbf{p}) = [\mathbf{h}_{t,1}^{(l)}(\mathbf{p}), \dots, \mathbf{h}_{t,N_{sc}}^{(l)}(\mathbf{p})] \in \mathbb{C}^{N_r \times N_{sc}}$.

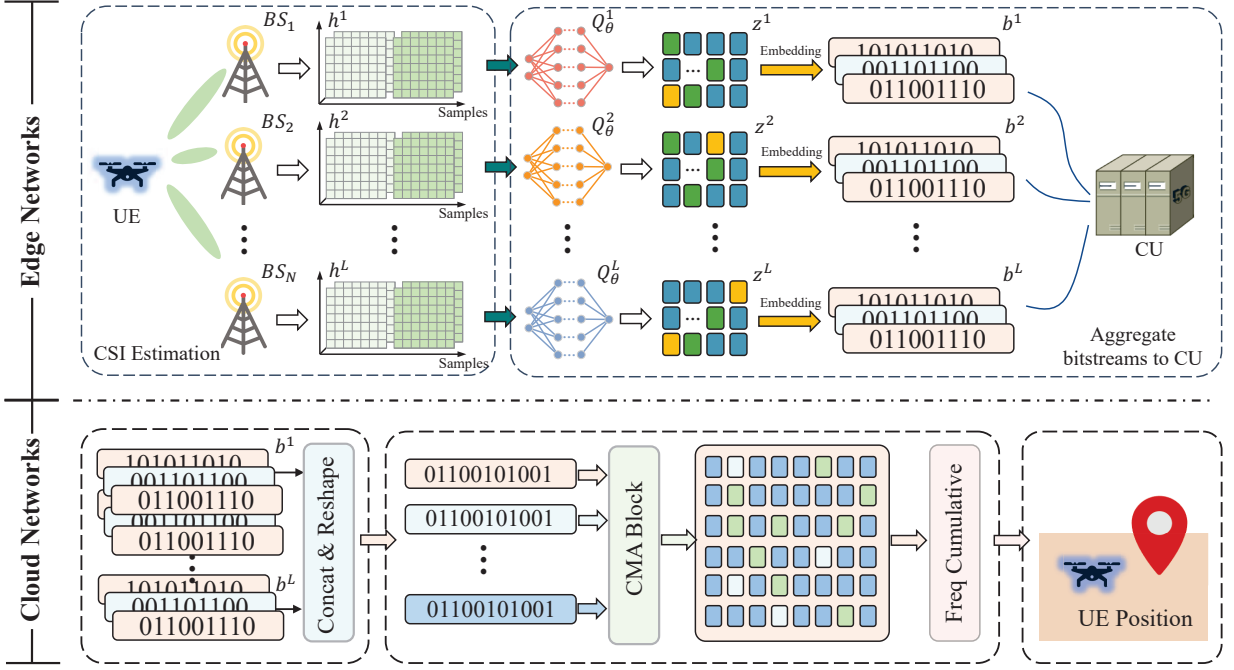


Fig. 2: The proposed ECC positioning framework. At the edges, each BS estimates the local CSI from uplink and transform it to quantized latent embedding. At the cloud, the CU infers 3D positioning of UE directly from the received bitstreams.

B. Edge-Cloud Cooperative Positioning Framework

As illustrated in Fig. 2, we propose an edge-cloud cooperative positioning (ECC) framework that enables fronthaul-efficient multi-BS cooperation for 3D localization. Within the ECC framework, each BS operates as an edge node that acquires uplink pilot signals, estimates the wideband multi-antenna channel state information (CSI), and compresses the estimated CSI into a fixed-length fronthaul bitstream under an explicit payload budget. The CU aggregates the received bitstreams, together with optional link-quality side information, from all BSs and directly infers the three-dimensional (3D) position of a single-antenna user equipment (UE).

We consider uplink pilot transmission from a single-antenna UE to L distributed BSs. At time slot $t \in \{1, \dots, T\}$, the received pilot observation at the l -th BS is

$$\mathbf{Y}_t^{(l)} = \mathbf{H}_t^{(l)}(\mathbf{p}) \mathbf{X}_p + \mathbf{N}_t^{(l)}, \quad (2)$$

where $\mathbf{Y}_t^{(l)} \in \mathbb{C}^{N_r \times N_{sc}}$ collects the received pilot symbols on N_{sc} subcarriers, $\mathbf{H}_t^{(l)}(\mathbf{p}) \in \mathbb{C}^{N_r \times N_{sc}}$ is the frequency-domain MIMO channel, $\mathbf{X}_p \triangleq \text{diag}(x_1, \dots, x_{N_{sc}}) \in \mathbb{C}^{N_{sc} \times N_{sc}}$ contains known pilot symbols with $x_n \neq 0$, and $\mathbf{N}_t^{(l)} \in \mathbb{C}^{N_r \times N_{sc}}$ is additive noise whose entries are i.i.d. $\mathcal{CN}(0, \sigma^2)$.¹ For notational simplicity, we assume the same diagonal pilot matrix \mathbf{X}_p is used for all t ; allowing slot-dependent pilots only replaces x_n by $x_{t,n}$ in Eq. (3)–Eq. (4).

Under the standard OFDM assumption that inter-carrier interference is negligible, and since \mathbf{X}_p is diagonal, the observation decouples across subcarriers. For each subcarrier

¹For notational simplicity we assume a common noise variance σ^2 across antennas and subcarriers; the proposed framework does not rely on this simplification.

n , let $\mathbf{y}_{t,n}^{(l)} \in \mathbb{C}^{N_r}$ and $\mathbf{h}_{t,n}^{(l)} \in \mathbb{C}^{N_r}$ denote the n -th columns of $\mathbf{Y}_t^{(l)}$ and $\mathbf{H}_t^{(l)}$, respectively. Then

$$\mathbf{y}_{t,n}^{(l)} = x_n \mathbf{h}_{t,n}^{(l)}(\mathbf{p}) + \mathbf{n}_{t,n}^{(l)}. \quad (3)$$

Each BS performs local channel estimation based on Eq. (2). To distinguish deterministic geometric dependence from random small-scale effects, we interpret $\mathbf{h}_{t,n}^{(l)}(\mathbf{p})$ as one realization of a random vector conditioned on \mathbf{p} . For tractable minimum mean-square error (MMSE) estimation, we employ a zero-mean circularly symmetric complex Gaussian (CSCG) second-order model characterized by a covariance matrix, which serves as a surrogate prior that can be estimated from long-term measurements. Under the CSCG model, the LMMSE estimator coincides with the Bayesian MMSE estimator. We emphasize that this CSCG prior is used as a tractable second-order surrogate for channel estimation and does not require the physical multipath channel to be exactly Gaussian. In the derivation below, we suppress the explicit conditioning on \mathbf{p} for notational convenience.

Assume $\mathbf{h}_{t,n}^{(l)} \sim \mathcal{CN}(\mathbf{0}, \mathbf{R}_{h,n}^{(l)})$ with covariance $\mathbf{R}_{h,n}^{(l)} \triangleq \mathbb{E}[\mathbf{h}_{t,n}^{(l)}(\mathbf{h}_{t,n}^{(l)})^H]$. We assume that BS l has access to an estimate of $\mathbf{R}_{h,n}^{(l)}$, e.g., via long-term averaging or offline calibration. The LMMSE estimator admits the standard form $\hat{\mathbf{h}}_{t,n}^{(l)} = \mathbf{C}_{hy} \mathbf{C}_{yy}^{-1} \mathbf{y}_{t,n}^{(l)}$, where $\mathbf{C}_{hy} \triangleq \mathbb{E}[\mathbf{h}_{t,n}^{(l)}(\mathbf{y}_{t,n}^{(l)})^H]$ and $\mathbf{C}_{yy} \triangleq \mathbb{E}[\mathbf{y}_{t,n}^{(l)}(\mathbf{y}_{t,n}^{(l)})^H]$. From (3) and the independence of $\mathbf{h}_{t,n}^{(l)}$ and $\mathbf{n}_{t,n}^{(l)}$, we obtain $\mathbf{C}_{hy} = x_n^* \mathbf{R}_{h,n}^{(l)}$ and $\mathbf{C}_{yy} = |x_n|^2 \mathbf{R}_{h,n}^{(l)} + \sigma^2 \mathbf{I}_{N_r}$, which yields

$$\hat{\mathbf{h}}_{t,n}^{(l)} = \mathbf{R}_{h,n}^{(l)} x_n^* \left(|x_n|^2 \mathbf{R}_{h,n}^{(l)} + \sigma^2 \mathbf{I}_{N_r} \right)^{-1} \mathbf{y}_{t,n}^{(l)}. \quad (4)$$

When $\mathbf{R}_{h,n}^{(l)} \propto \mathbf{I}_{N_r}$ and the pilots have constant modulus, (4) reduces to a scaled matched filter (pilot correlation); more

generally it exploits spatial correlation encoded by $\mathbf{R}_{h,n}^{(l)}$.

Stacking $\{\widehat{\mathbf{h}}_{t,n}^{(l)}\}_{n=1}^{N_{sc}}$ yields the estimated CSI matrix $\widehat{\mathbf{H}}_t^{(l)} \in \mathbb{C}^{N_r \times N_{sc}}$. We collect $\{\widehat{\mathbf{H}}_t^{(l)}\}_{t=1}^T$ into a third-order matrix

$$\widehat{\mathbf{H}}^{(l)} \in \mathbb{C}^{T \times N_r \times N_{sc}}, \quad (5)$$

whose t -th slice satisfies $\widehat{\mathbf{H}}_t^{(l)} = \widehat{\mathbf{H}}^{(l)}[t, :, :]$. Similarly, stacking $\{\widehat{\mathbf{H}}^{(l)}\}_{l=1}^L$ yields

$$\widehat{\mathbf{H}} \in \mathbb{C}^{L \times T \times N_r \times N_{sc}}, \quad (6)$$

where $\widehat{\mathbf{H}}^{(l)} = \widehat{\mathbf{H}}[l, :, :, :]$ $\forall l$.

C. Side Information Extraction and Fronthaul Compression

Directly compressing raw CSI is challenging due to large dynamic-range variations across users and BSs. Moreover, for cooperative fusion, the CU benefits from additional information such as received signal strength (RSS), which we define as lightweight side information. Therefore, we adopt a *decoupled* fronthaul message consisting of (i) a normalized CSI-derived embedding and (ii) a scalar gain indicator.

Specifically, the l -th BS extracts a scalar channel-quality indicator

$$g^{(l)} \triangleq \|\widehat{\mathbf{H}}^{(l)}\|_F, \quad (7)$$

where for any complex-valued matrix \mathbf{A} , $\|\mathbf{A}\|_F \triangleq (\sum |A|^2)^{1/2}$ and equivalently $\|\mathbf{A}\|_F = \|\text{vec}(\mathbf{A})\|_2$, with $\text{vec}(\cdot)$ denoting any fixed vectorization that stacks all entries into a column vector. Let $\widehat{h}_{t,m,n}^{(l)}$ denote the (t, m, n) -th entry of $\widehat{\mathbf{H}}^{(l)}$. Equivalently, $g^{(l)} = \left(\sum_{t=1}^T \sum_{m=1}^{N_r} \sum_{n=1}^{N_{sc}} |\widehat{h}_{t,m,n}^{(l)}|^2\right)^{1/2}$. The BS normalizes its CSI as

$$\overline{\mathbf{H}}^{(l)} \triangleq \frac{\widehat{\mathbf{H}}^{(l)}}{g^{(l)} + \epsilon}, \quad (8)$$

where $\epsilon > 0$ prevents division by zero and improves numerical robustness for very weak links. This normalization reduces sensitivity to large-scale fading, while $g^{(l)}$ serves as a coarse proxy for link strength, up to the bias introduced by estimation noise. If the gain indicator is transmitted using B_g bits, let $\widehat{g}^{(l)}$ denote its decoded value at the CU; if it is transmitted without quantization, then $\widehat{g}^{(l)} = g^{(l)}$.

In practical multi-antenna receivers, residual oscillator impairments and hardware mismatches can induce an unknown phase rotation that is approximately common across antennas for a given (t, n) . Since such rotations are nuisance factors for fingerprint-based learning, we perform per- (t, n) phase stabilization using a reference antenna.

Let $\overline{h}_{t,m,n}^{(l)}$ denote the entry of $\overline{\mathbf{H}}^{(l)}$ at time slot t , antenna m , and subcarrier n . To improve numerical robustness, we select a snapshot-wise reference antenna as

$$m_0^{(l)} \triangleq \arg \max_{m \in \{1, \dots, N_r\}} \frac{1}{TN_{sc}} \sum_{t=1}^T \sum_{n=1}^{N_{sc}} |\overline{h}_{t,m,n}^{(l)}|^2, \quad (9)$$

where ties (if any) are broken by choosing the smallest maximizing index. Let $\epsilon_{\angle} > 0$ be a small threshold and define the reference phase

$$\phi_{t,n}^{(l)} \triangleq \begin{cases} \angle \overline{h}_{t,m_0^{(l)},n}^{(l)}, & |\overline{h}_{t,m_0^{(l)},n}^{(l)}| \geq \epsilon_{\angle}, \\ 0, & \text{otherwise.} \end{cases} \quad (10)$$

We then perform phase stabilization as

$$\widetilde{h}_{t,m,n}^{(l)} = \overline{h}_{t,m,n}^{(l)} \exp(-j\phi_{t,n}^{(l)}), \quad (11)$$

and denote the resulting phase-stabilized CSI by $\widetilde{\mathbf{H}}^{(l)}$. For those (t, n) such that $|\overline{h}_{t,m_0^{(l)},n}^{(l)}| \geq \epsilon_{\angle}$, the stabilization preserves relative phases across antennas:

$$\angle \widetilde{h}_{t,m,n}^{(l)} - \angle \widetilde{h}_{t,m_0^{(l)},n}^{(l)} = \angle \overline{h}_{t,m,n}^{(l)} - \angle \overline{h}_{t,m_0^{(l)},n}^{(l)}. \quad (12)$$

Most deep learning backbones used in this work operate on real-valued matrices. We represent complex CSI by stacking real and imaginary parts as two channels. Define the stacking operator $\mathcal{S} : \mathbb{C}^{T \times N_r \times N_{sc}} \rightarrow \mathbb{R}^{T \times N_r \times N_{sc} \times 2}$ element-wise by

$$\begin{aligned} [\mathcal{S}(\mathbf{A})]_{t,m,n,1} &= \Re\{A_{t,m,n}\}, \\ [\mathcal{S}(\mathbf{A})]_{t,m,n,2} &= \Im\{A_{t,m,n}\}. \end{aligned} \quad (13)$$

Accordingly, for any $\mathbf{B} \in \mathbb{R}^{T \times N_r \times N_{sc} \times 2}$, define $\mathcal{S}^{-1}(\mathbf{B}) \in \mathbb{C}^{T \times N_r \times N_{sc}}$ by $[\mathcal{S}^{-1}(\mathbf{B})]_{t,m,n} = B_{t,m,n,1} + jB_{t,m,n,2}$.

We also define a reshape operator $\mathcal{R}(\cdot)$ that flattens the time and antenna dimensions into a single index while preserving the frequency and channel dimensions. Specifically, for $\mathbf{B} \in \mathbb{R}^{T \times N_r \times N_{sc} \times 2}$, define $\mathbf{X} = \mathcal{R}(\mathbf{B}) \in \mathbb{R}^{(TN_r) \times N_{sc} \times 2}$ by

$$X_{(t-1)N_r+m, n, c} = B_{t,m,n,c}, \quad (14)$$

where $t = 1, \dots, T$, $m = 1, \dots, N_r$, $n = 1, \dots, N_{sc}$, $c \in \{1, 2\}$. Let $\mathcal{R}^{-1}(\cdot)$ denote the inverse mapping defined by the inverse index relation. With these operators, the BS input is

$$\mathbf{X}^{(l)} \triangleq \mathcal{R}(\mathcal{S}(\widetilde{\mathbf{H}}^{(l)})) \in \mathbb{R}^{(TN_r) \times N_{sc} \times 2}. \quad (15)$$

An encoder deployed at BS l maps $\mathbf{X}^{(l)}$ to a frequency-aligned latent matrix

$$\mathbf{z}^{(l)} = E_{\theta^{(l)}}(\mathbf{X}^{(l)}) \in \mathbb{R}^{N_{sc} \times d_z}, \quad (16)$$

where the n -th row $\mathbf{z}_n^{(l)} \in \mathbb{R}^{d_z}$ serves as the token associated with subcarrier n . For fronthaul packing, we adopt a frequency-ordered vectorization by concatenating the row tokens:

$$\mathbf{z}^{(l)} \triangleq [(\mathbf{z}_1^{(l)})^T, \dots, (\mathbf{z}_{N_{sc}}^{(l)})^T]^T \in \mathbb{R}^D, \quad D \triangleq N_{sc}d_z. \quad (17)$$

Equivalently, $\mathbf{Z}^{(l)}$ is obtained by reshaping $\mathbf{z}^{(l)}$ into N_{sc} rows and d_z columns in the same order. The indices $\{q_i^{(l)}\}_{i=1}^D$ defined below are ordered consistently with Eq. (17).

The embedding process is performed on the latent space. Instead of traditional signal quantization aimed at waveform reconstruction, the continuous latent vector $\mathbf{z}^{(l)}$ is embedded into a digital bitstream to facilitate semantic information transmission. This process functions as a feature tokenizer, mapping continuous features to discrete codes that the cloud network can interpret as input tokens.

Specifically, the discretization operator $\mathcal{Q}_c(\cdot)$ is employed to map the real and imaginary components of the latent features onto a finite codebook. Assuming an embedding resolution of Q bits, the latent vector $\mathbf{z}^{(l)}$ is converted into the bitstream $\hat{\mathbf{b}}^{(l)}$ via:

$$\hat{\mathbf{b}}^{(l)} = \mathcal{Q}_c(\mathbf{z}^{(l)}) = \mathcal{Q}(\Re\{\mathbf{z}^{(l)}\}) + j\mathcal{Q}(\Im\{\mathbf{z}^{(l)}\}) \quad (18)$$

where $Q(\cdot)$ denotes the discretization function, $\Re\{\cdot\}$ and $\Im\{\cdot\}$ denote the real and imaginary parts of a complex number, respectively. To be specific, the midrise uniform method is adopted, and each element y of $\mathbf{z}^{(l)}$ is embedded as follows:

$$Q(y) = \begin{cases} \frac{(2^Q-1)\Delta}{2}, & y > (2^Q-1)\Delta \\ \lfloor \frac{y}{\Delta} \rfloor \Delta + \frac{\Delta}{2}, & -\frac{(2^Q-1)\Delta}{2} \leq y \leq \frac{(2^Q-1)\Delta}{2} \\ -\frac{(2^Q-1)\Delta}{2}, & y < -\frac{(2^Q-1)\Delta}{2} \end{cases} \quad (19)$$

with Δ being the embedding step size. The optimal choice of Δ depends on the statistical distribution of the channel coefficients and the desired trade-off between fronthaul overhead and positioning error.

D. Centralized Positioning from Embedded Bitstreams

The CU receives $\{\hat{\mathbf{b}}^{(l)}, \hat{g}^{(l)}\}_{l=1}^L$ from all BSs and aggregates the embeddings by concatenation in a predetermined order (e.g., by BS index),

$$\hat{\mathbf{b}} \triangleq [\hat{\mathbf{b}}^{(1)}, \hat{\mathbf{b}}^{(2)}, \dots, \hat{\mathbf{b}}^{(L)}]. \quad (20)$$

It also forms the gain vector $\hat{\mathbf{g}} \triangleq [\hat{g}^{(1)}, \dots, \hat{g}^{(L)}]^T$. A cloud-side positioning network $F_\phi(\cdot)$ with parameters ϕ then estimates the UE position

$$\hat{\mathbf{p}} = F_\phi(\hat{\mathbf{b}}, \hat{\mathbf{g}}), \quad \hat{\mathbf{p}} = [\hat{x}, \hat{y}, \hat{z}]^T \in \mathbb{R}^3. \quad (21)$$

Depending on implementation, $F_\phi(\cdot)$ may take the raw bit vector $\hat{\mathbf{b}}$ as input or first unpack and dequantize it into $\{\hat{\mathbf{z}}^{(l)}\}_{l=1}^L$; both choices correspond to the same fronthaul payload.

III. ECC ARCHITECTURE: EDGE BITSTREAM EMBEDDING, RELIABILITY-AWARE CLOUD FUSION, AND QUANTIZATION-AWARE TRAINING

In this section, we detail the proposed ECC architecture and its quantization-aware two-stage training procedure. We first present the edge-side residual SegNet embedding network that produces quantization-friendly latent representations. We then introduce the cloud-side positioning network that couples channel-masked attention (CMA) for multi-BS fusion with a frequency evidence accumulation module for wideband regression. Finally, we provide a training strategy that stabilizes representation learning and enables end-to-end positioning through the non-differentiable quantization bottleneck.

A. Edge Embedding: Residual SegNet Autoencoder and Quantization Bottleneck

At BS $l \in \{1, \dots, L\}$, uplink pilots collected over T time slots yield an estimated CSI $\hat{\mathbf{H}}^{(l)}$. The BS performs gain extraction and normalization, and then phase stabilization according to Eq.(7) – Eq.(11). The stabilized CSI is reshaped into a real-valued matrix and mapped by an encoder to a compact frequency-aligned latent matrix $\mathbf{Z}^{(l)} \in \mathbb{R}^{N_{sc} \times d_z}$ according to Eq.(16). The frequency-ordered latent vector $\mathbf{z}^{(l)} \in \mathbb{R}^D$ is formed as in Eq.(17) and then uniformly quantized with Q bits per coefficient using (19), producing a *fixed-length* fronthaul bitstream of exactly DQ bits. Optionally, the scalar indicator

$g^{(l)}$ is encoded and transmitted as side information; the CU uses its decoded value $\hat{g}^{(l)}$.

To avoid requiring labeled positions at each BS during initialization, we employ a residual SegNet-style autoencoder [48] for self-supervised local training (Stage I).

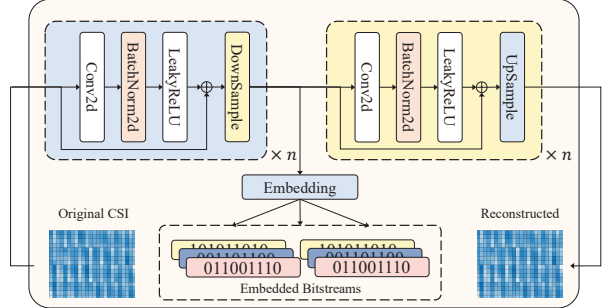


Fig. 3: The proposed embedding network (Res-SegNet).

As shown in Fig. 3, the encoder contains convolutional blocks with residual shortcuts, followed by down-sampling operations that reduce feature resolution and produce a compact latent. The decoder mirrors the encoder with up-sampling and residual blocks to reconstruct the *preprocessed* CSI matrix (after gain normalization and phase stabilization).

Let $\mathbf{h}_{\text{CSI}}^{(l)} \triangleq \text{vec}(\tilde{\mathbf{H}}^{(l)})$ and $\hat{\mathbf{h}}_{\text{CSI}}^{(l)} \triangleq \text{vec}(\hat{\mathbf{H}}^{(l)})$ denote the vectorized phase-stabilized CSI matrix and its reconstruction, respectively, where $\text{vec}(\cdot)$ stacks all entries in the same fixed order for both matrices. We maximize their normalized correlation; equivalently, we minimize its negative value:

$$\mathcal{L}_{\text{cos}} = -\frac{|\mathbf{h}_{\text{CSI}}^{(l)} \mathbf{h}_{\text{CSI}}^{(l)}|}{\|\mathbf{h}_{\text{CSI}}^{(l)}\|_2 \|\hat{\mathbf{h}}_{\text{CSI}}^{(l)}\|_2 + \epsilon_{\text{cos}}}, \quad (22)$$

where $\epsilon_{\text{cos}} > 0$ ensures numerical stability.

B. Cloud Positioning Network: CMA Fusion and Frequency Evidence Accumulation

Upon receiving $\{\hat{\mathbf{b}}^{(l)}, \hat{g}^{(l)}\}_{l=1}^L$, the CU performs centralized inference. The positioning network consists of CMA for multi-BS fusion and frequency evidence accumulation for wideband regression.

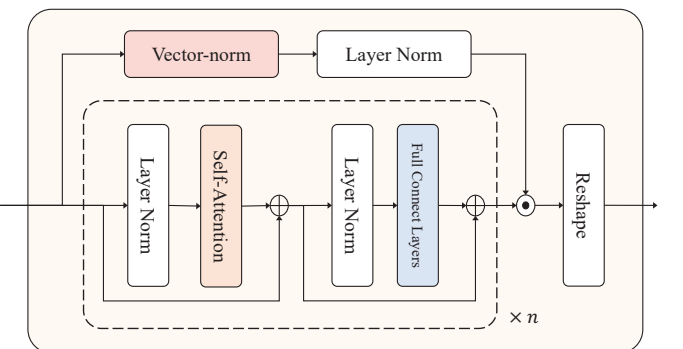


Fig. 4: The proposed CMA mechanism.

1) *Channel-Masked Attention (CMA)*: As shown in Fig. 4, the CMA mechanism is designed to integrate a standard

Transformer encoder backbone with a parallel normalization gating mechanism. Let $\hat{\mathbf{g}} = [\hat{g}^{(1)}, \dots, \hat{g}^{(L)}]^T$ be the gain vector available at the CU. We define normalized weights

$$\mathbf{m} = \text{softmax}(\beta \hat{\mathbf{g}}) \in \mathbb{R}^L, \quad (23)$$

where $\beta > 0$ is a temperature parameter.

For each BS l , we fuse $\{\mathbf{b}^{(l)}\}_{l=1}^L$ using a Transformer-style attention layer. To obtain a single fused representation per subcarrier, we prepend a learnable fusion parameters $\mathbf{b}^{(0)} \in \mathbb{R}^{N_{sc}d}$ (shared across l) and construct

$$\mathbf{B}_l = [(\mathbf{b}^{(0)})^T, (\mathbf{b}_n^{(1)})^T, \dots, (\mathbf{b}_n^{(L)})^T]^T \in \mathbb{R}^{(L+1) \times N_{sc}d}. \quad (24)$$

Define scaled dot-product attention as

$$\text{Attn}(\mathbf{Q}, \mathbf{K}, \mathbf{V}) = \text{softmax}\left(\frac{\mathbf{Q}\mathbf{K}^T}{\sqrt{d_k}}\right)\mathbf{V}, \quad (25)$$

where $d_k = N_{sc}d$ in our implementation and the softmax is applied row-wise. We take $\mathbf{W}_Q, \mathbf{W}_K, \mathbf{W}_V \in \mathbb{R}^{N_{sc}d \times N_{sc}d}$ and apply channel-aware value gating by defining

$$\mathbf{M} \triangleq \text{diag}([1, m_1, \dots, m_L]) \in \mathbb{R}^{(L+1) \times (L+1)}, \quad (26)$$

and computing

$$\mathbf{O}_l = \text{Attn}(\mathbf{B}_l \mathbf{W}_Q, \mathbf{B}_l \mathbf{W}_K, \mathbf{M} \mathbf{B}_l \mathbf{W}_V) \in \mathbb{R}^{(L+1) \times N_{sc}d}. \quad (27)$$

The fused presentation for distributed BS is taken as the last-row output corresponding to the output:

$$\{\mathbf{v}_n\}_{n=1}^{N_{sc}} \triangleq [\mathbf{O}_l]_{(L+1),:} \in \mathbb{R}^{N_{sc}d}. \quad (28)$$

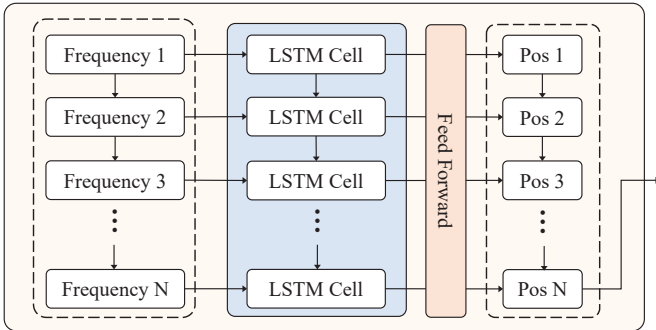


Fig. 5: The proposed frequency evidence accumulation mechanism.

2) *Frequency Evidence Accumulation: Physical Motivation and Sequence Model:* As shown in Fig. 5, the frequency accumulation network treats the concatenated time and antenna dimension as the initial feature token and subcarrier dimensions as the sequence length. To motivate frequency-ordered processing, consider a standard wideband multipath model for the uplink channel vector at BS l (time index omitted for simplicity):

$$\mathbf{h}^{(l)}(f) \approx \sum_{k=1}^{K_l} \alpha_k^{(l)} \mathbf{a}_r^{(l)}(\vartheta_k^{(l)}, \varphi_k^{(l)}) e^{-j2\pi f \tau_k^{(l)}}, \quad (29)$$

where $\alpha_k^{(l)} \in \mathbb{C}$ is the complex path gain, $\mathbf{a}_r^{(l)}(\cdot)$ is the receive array response, and $\tau_k^{(l)}$ is the path delay. Sampling (29) at OFDM subcarrier frequencies $f_n = f_0 + (n-1)\Delta f$ yields

$$\begin{aligned} \mathbf{h}_n^{(l)} &\triangleq \mathbf{h}^{(l)}(f_n) \\ &\approx \sum_{k=1}^{K_l} \alpha_k^{(l)} \mathbf{a}_r^{(l)}(\vartheta_k^{(l)}, \varphi_k^{(l)}) e^{-j2\pi f_0 \tau_k^{(l)}} e^{-j2\pi(n-1)\Delta f \tau_k^{(l)}}. \end{aligned} \quad (30)$$

The subcarrier-independent factor $e^{-j2\pi f_0 \tau_k^{(l)}}$ can be absorbed into $\alpha_k^{(l)}$; we keep it explicit for clarity. For each path component, the factor $e^{-j2\pi(n-1)\Delta f \tau_k^{(l)}}$ varies regularly with n , implying structured dependencies across subcarriers. In particular, for a single path component, the phase progression between adjacent subcarriers satisfies

$$\frac{e^{-j2\pi(n-1)\Delta f \tau_k^{(l)}}}{e^{-j2\pi(n-2)\Delta f \tau_k^{(l)}}} = e^{-j2\pi \Delta f \tau_k^{(l)}}, \quad n = 2, \dots, N_{sc}, \quad (31)$$

which is independent of n . When frequency subsampling is applied, the token index n refers to the retained subcarriers and (31) holds with Δf replaced by the effective spacing between adjacent retained subcarriers, denoted by Δf_{eff} .

We feed the fused presentation sequence $\{\mathbf{v}_n\}_{n=1}^{N_{sc}}$ into an LSTM:

$$(\mathbf{s}_n, \mathbf{c}_n) = \text{LSTM}(\mathbf{v}_n, \mathbf{s}_{n-1}, \mathbf{c}_{n-1}), \quad n = 1, \dots, N_{sc}, \quad (32)$$

with $\mathbf{s}_0 = \mathbf{0}$ and $\mathbf{c}_0 = \mathbf{0}$. A regression head maps each hidden state to an intermediate 3D estimate:

$$\hat{\mathbf{p}}_n = f_{\text{reg}}(\mathbf{s}_n) \in \mathbb{R}^3, \quad n = 1, \dots, N_{sc}, \quad (33)$$

and the final estimate is $\hat{\mathbf{p}} = \hat{\mathbf{p}}_{N_{sc}}$.

During Stage II, we train the CU network and BS encoders using a weighted mean squared error (WMSE):

$$\mathcal{L}_{\text{pos}} = \sum_{i=1}^{N_{sc}} w_i \|\mathbf{p} - \hat{\mathbf{p}}_i\|_2^2, \quad w_i \triangleq \frac{2i}{N_{sc}(N_{sc}+1)}, \quad (34)$$

where $\{w_i\}$ satisfies $w_i \geq 0$ and $\sum_{i=1}^{N_{sc}} w_i = 1$, thus emphasizing later estimates.

C. Quantization-Aware Two-Stage Training

The ECC network is trained under an explicit, fixed-length fronthaul constraint. A direct end-to-end optimization from scratch is often unstable because the CU regressor must learn to interpret quantized embeddings while the BS encoders are still producing non-robust features. We therefore adopt a two-stage training strategy that decouples *representation stabilization* from *task-oriented joint training*.

Stage I (self-supervised local training). At each BS l , we initialize a residual SegNet-style autoencoder using unlabeled CSI snapshots. The encoder-decoder parameters $(\theta^{(l)}, \psi^{(l)})$ are optimized by minimizing the cosine-similarity loss in (22), after preprocessing in (7)–(15). During this stage, the quantizer is bypassed and the bottleneck remains continuous, which improves optimization stability. After Stage I, the decoder is discarded and only the encoder parameters $\theta^{(l)}$ are retained.

Stage II (end-to-end joint training). We jointly train all BS encoders $\{\theta^{(l)}\}_{l=1}^L$ together with the CU network parameters

Algorithm 1 Stage I: Self-supervised Local Training at BS l (executed independently for $l = 1, \dots, L$)

Require: Unlabeled CSI $\{\widehat{\mathbf{H}}_i^{(l)}\}_{i=1}^{N_l}$; preprocessing (7)–(15); encoder $E_{\theta^{(l)}}$; decoder $D_{\psi^{(l)}}$; learning rate α ; iterations K .

- 1: Initialize $\theta^{(l)}$ and $\psi^{(l)}$.
- 2: **for** $k = 1$ to K **do**
- 3: Sample a mini-batch $\mathcal{B} \subset \{\widehat{\mathbf{H}}_i^{(l)}\}$.
- 4: Preprocess each $\widehat{\mathbf{H}} \in \mathcal{B}$ to obtain network input \mathbf{X} and phase-stabilized CSI $\widehat{\mathbf{H}}$.
- 5: Forward: $\widehat{\mathbf{X}} \leftarrow D_{\psi^{(l)}}(E_{\theta^{(l)}}(\mathbf{X}))$.
- 6: Recover $\widehat{\mathbf{H}} \leftarrow \mathcal{S}^{-1}(\mathcal{R}^{-1}(\widehat{\mathbf{X}}))$.
- 7: Compute \mathcal{L}_{cos} by (22) with $\mathbf{h}_{\text{CSI}} = \text{vec}(\widetilde{\mathbf{H}})$ and $\widehat{\mathbf{h}}_{\text{CSI}} = \text{vec}(\widehat{\mathbf{H}})$.
- 8: Update $(\theta^{(l)}, \psi^{(l)}) \leftarrow (\theta^{(l)}, \psi^{(l)}) - \alpha \nabla_{(\theta^{(l)}, \psi^{(l)})} \mathcal{L}_{\text{cos}}$.
- 9: **end for**
- 10: **Output:** Local trained encoder parameters $\theta^{(l)}$ (decoder $D_{\psi^{(l)}}$ is discarded after Stage I).

ϕ using labeled positions and the WMSE loss in (34). In the forward pass, each BS latent is quantized using (19) to satisfy the fixed payload of DQ bits per BS. Since uniform quantization is non-differentiable, we backpropagate through the quantizer using the straight-through estimator (STE):

$$\frac{\partial \mathcal{Q}(y)}{\partial y} \approx \begin{cases} 1, & |y| \leq A, \\ 0, & |y| > A. \end{cases} \quad (35)$$

Algorithms 1 and 2 summarize Stage I and Stage II, respectively. After training, each BS runs only preprocessing (7)–(15), the encoder $E_{\theta^{(l)}}(\cdot)$, and the Q -bit quantizer, while the CU runs the token projection, CMA fusion, frequency evidence accumulation, and regression head to produce $\widehat{\mathbf{p}}$.

IV. SIMULATION RESULTS

A. Simulation Setup and Evaluation Protocol

We evaluate the proposed edge–cloud cooperative (ECC) positioning framework in a ray-traced urban environment around the Yuquan campus of Zhejiang University, where $L = 6$ distributed BSs are deployed for cooperative CSI acquisition (Fig. 6). Wideband uplink MIMO–OFDM channels are generated using the 5G NR-compliant ray-tracing pipeline in the Sionna library [49], which adopts a shooting-and-bouncing-rays procedure and includes up to 10 specular reflections. The BS locations follow real-world site records obtained from OpenCellID [50]. The UE horizontal position is uniformly sampled within a $220 \text{ m} \times 300 \text{ m}$ region, and the UE height is uniformly sampled from $[0, 30] \text{ m}$ to emulate both ground and low-altitude users in urban scenarios.

a) NR numerology and time–frequency subsampling.:

We consider a carrier frequency $f_c = 3.5 \text{ GHz}$ and bandwidth 20 MHz with subcarrier spacing (SCS) $\Delta f = 60 \text{ kHz}$. The full NR grid contains $N_{sc}^{\text{full}} = 288$ subcarriers, corresponding to $N_{sc}^{\text{full}}/12 = 24$ resource blocks (RBs) with 12 subcarriers per RB. To reduce CSI dimensionality and emulate that only

Algorithm 2 Stage II: End-to-End Joint Training of the ECC Network

Require: Labeled snapshots $\{(\{\widehat{\mathbf{H}}_i^{(l)}\}_{i=1}^L, \mathbf{p}_i)\}_{i=1}^N$; preprocessing (7)–(15); trained encoders $\{E_{\theta^{(l)}}\}_{l=1}^L$; CU network F_ϕ ; quantizer $\mathcal{Q}(\cdot)$ defined by (19) with STE (35); learning rate α ; iterations K .

- 1: Initialize ϕ and set $\theta^{(l)}$ from Stage I for all l .
- 2: **for** $k = 1$ to K **do**
- 3: Sample a mini-batch \mathcal{B} of labeled snapshots.
- 4: **Edge forward:** for each BS l , preprocess $\widehat{\mathbf{H}}^{(l)}$ to obtain $\mathbf{X}^{(l)}$ and $g^{(l)}$, set $\widehat{g}^{(l)} \leftarrow g^{(l)}$ (or apply a fixed B_g -bit encoding/decoding if used), encode $\mathbf{Z}^{(l)} \leftarrow E_{\theta^{(l)}}(\mathbf{X}^{(l)})$, and quantize element-wise $\widehat{\mathbf{Z}}^{(l)} \leftarrow \mathcal{Q}(\mathbf{Z}^{(l)})$.
- 5: **Cloud forward:** form $\widehat{\mathbf{g}} = [\widehat{g}^{(1)}, \dots, \widehat{g}^{(L)}]^T$ and compute \mathbf{m} by (23), fuse via CMA (27)–(28), accumulate across frequency via (32), and predict $\{\widehat{\mathbf{p}}_n\}_{n=1}^{N_{sc}}$ via (33).
- 6: Compute \mathcal{L}_{pos} using (34).
- 7: Backpropagate through $\mathcal{Q}(\cdot)$ using STE (35) and update $\phi \leftarrow \phi - \alpha \nabla_\phi \mathcal{L}_{\text{pos}}$, $\theta^{(l)} \leftarrow \theta^{(l)} - \alpha \nabla_{\theta^{(l)}} \mathcal{L}_{\text{pos}}$ for all l .
- 8: **end for**
- 9: **Output:** Joint trained encoders $\{E_{\theta^{(l)}}\}_{l=1}^L$ and CU network F_ϕ .

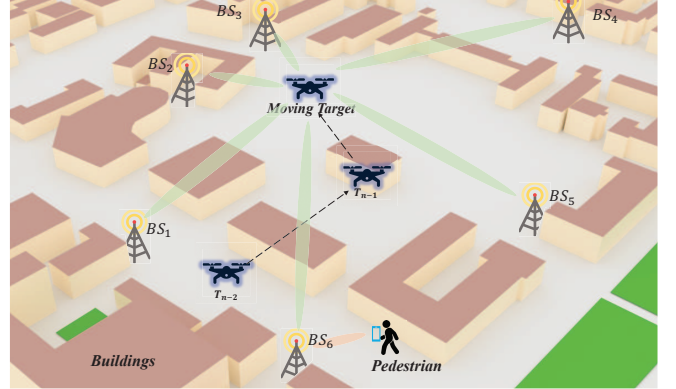


Fig. 6: Ray-traced 3D urban scene used for CSI generation.

sparse time–frequency resources are used for positioning, we retain one subcarrier per RB (a 12-subcarrier stride), yielding an effective $N_{sc} = 24$ subcarriers for CSI processing. In time, we retain every other subframe (downsampling factor 2), resulting in T effective time slots per positioning snapshot. Unless otherwise stated, N_{sc} denotes the effective number of subcarriers after subsampling. As we retain one subcarrier per RB, the effective frequency spacing between adjacent retained subcarriers is $\Delta f_{\text{eff}} = 12\Delta f$, and the index n in the proposed frequency-ordered processing refers to these retained subcarriers ordered by frequency.

b) *CSI estimation and preprocessing.*: The main parameters are summarized in Table I. At each BS, CSI is estimated from uplink pilots using the per-subcarrier LMMSE estimator in Section II, forming an effective CSI matrix of size $T \times N_r \times N_{sc}$ per snapshot. Unless otherwise specified, each BS employs a 2×4 UPA ($N_r = 8$) with $0.5\lambda_c$ antenna spacing.

In simulations, $\mathbf{R}_{h,n}^{(l)}$ is estimated by long-term averaging over independently generated channel realizations at the same BS and subcarrier, and is kept fixed during both training and testing. In addition to physical-layer parameters, we explicitly list the embedding dimension and fronthaul-related settings that determine the payload.

TABLE I: Simulation and fronthaul-related parameters.

Parameter	Value
Number of BSs (L)	6
Carrier frequency (f_c)	3.5 GHz
Bandwidth	20 MHz
Subcarrier spacing (SCS) Δf	60 kHz
Full-grid subcarriers N_{sc}^{full}	288
Effective subcarriers used for positioning N_{sc}	24
Antenna array per BS	2×4 UPA ($N_r = 8$)
Antenna spacing	$0.5\lambda_c$
Max. specular reflections	10
Effective time slots per snapshot (T)	10
Latent dimension per subcarrier (d_z)	32
Latent vector length ($D = N_{sc}d_z$)	768
Quantization bits per coefficient (Q)	$\{4, 6, 8, 10\}$
Gain side-info bits (B_g)	32
Quantization step size (Δ)	calibrated on training set

c) Online sample generation and evaluation protocol.:

All training/validation/test samples are generated on the fly from the same simulator distribution. In each training epoch, we generate 3,000 fresh samples; validation is performed every fixed number of epochs using an independently generated set of 3,000 samples. Unless otherwise stated, all CDFs and summary statistics are computed over an independently generated test set. This protocol avoids repeated reuse of a finite dataset and reduces the risk of memorization under in-distribution evaluation.

d) Evaluation metrics.: For a test sample i , the 3D Euclidean localization error is

$$e_i \triangleq \|\mathbf{p}_i - \hat{\mathbf{p}}_i\|_2 \quad (\text{m}). \quad (36)$$

We report the mean error $\bar{e} \triangleq \frac{1}{N} \sum_{i=1}^N e_i$ and the 90th-percentile error e_{90} .

e) Fronthaul payload and ratio.: We measure fronthaul cost by assuming lossless CSI forwarding uses complex64 (64 bits/complex entry), i.e.,

$$B_{\text{CSI}} = 64 T N_r N_{sc} \text{ bits per BS per snapshot.} \quad (37)$$

The proposed fronthaul message contains a fixed-length embedding of DQ bits, where $D = N_{sc}d_z$ is the latent length and Q is the number of quantization bits per coefficient:

$$B_{\text{emb}} = DQ. \quad (38)$$

To match Table II, we report the fronthaul ratio excluding the optional gain side information:

$$\eta \triangleq \frac{B_{\text{emb}}}{B_{\text{CSI}}} = \frac{DQ}{64 T N_r N_{sc}}. \quad (39)$$

If the gain indicator is transmitted using B_g bits, the total per-BS payload is $B_{\text{tot}} = DQ + B_g$ and the corresponding total ratio is $\eta_{\text{tot}} = \frac{DQ + B_g}{64 T N_r N_{sc}}$.

B. Accuracy–Fronthaul Trade-off Under Different Quantization Resolutions

We first quantify the fundamental trade-off between fronthaul budget and positioning accuracy by varying the quantization resolution $Q \in \{4, 6, 8, 10\}$ bits per latent coefficient, while keeping the latent dimension D fixed (Table I). Table II summarizes the resulting mean error \bar{e} and 90th-percentile error e_{90} , as well as the fronthaul ratio η (excluding B_g). As Q increases, the quantization distortion in the latent representation decreases and the positioning accuracy improves, approaching the lossless-CSI reference.

TABLE II: Accuracy–fronthaul trade-off with Q bits per latent coefficient (fronthaul ratio η excludes B_g).

Embedding setting	Fronthaul ratio η	Mean 3D error \bar{e} (m)	90th perc. e_{90} (m)
Lossless CSI (no embedding)	100%	0.42	0.75
$Q = 10$	6.25%	0.48	0.83
$Q = 8$	5.00%	0.52	0.90
$Q = 6$	3.75%	0.54	0.92
$Q = 4$	2.50%	0.56	0.97

C. Convergence Analysis

We next examine training dynamics for (i) Stage I self-supervised embedding local training and (ii) Stage II end-to-end positioning joint training.

a) Stage I: embedding local training.: In each local training epoch, we generate 3,000 unlabeled CSI snapshots by sampling random UE locations in the deployment area. Every 15 epochs, we generate an independent validation set of 3,000 newly generated samples and record the reconstruction objective. Fig. 7 reports the negative cosine similarity in (22), which typically lies in $(-1, 0]$ due to $\epsilon_{\text{cos}} > 0$, where values closer to -1 indicate higher correlation magnitude. The objective decreases steadily and stabilizes after approximately 380 epochs, with training and validation curves closely matched under the same simulator distribution.

b) Stage II: end-to-end positioning joint training.: We train separate end-to-end models under $Q \in \{4, 6, 8, 10\}$ bits per latent coefficient. In each epoch, we generate 3,000 labeled samples; every 30 epochs we evaluate on an independently generated validation set of 3,000 samples. Fig. 8 shows the validation mean error during training. All models converge stably, and larger Q consistently yields lower validation error; for $Q = 10$, the mean error converges to approximately 0.5 m after around 210 epochs.

D. Impact of Different Training Strategies

We compare four training strategies: (i) **Joint Training (from scratch):** Stage I is skipped and the full model is trained end-to-end from random initialization with STE; (ii) **Local Training–Split Training:** Stage I is applied, then the encoder is frozen and only the CU network is trained; (iii) **Proposed Local Training–Joint Training:** Stage I local training followed by end-to-end joint training with STE, jointly updating BS encoders and the CU network; and (iv) **Raw CSI (no embedding):** training and inference with lossless CSI.

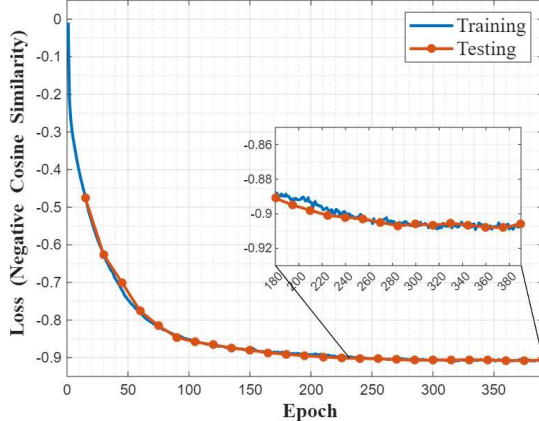


Fig. 7: Stage I reconstruction objective (negative cosine similarity in (22)).

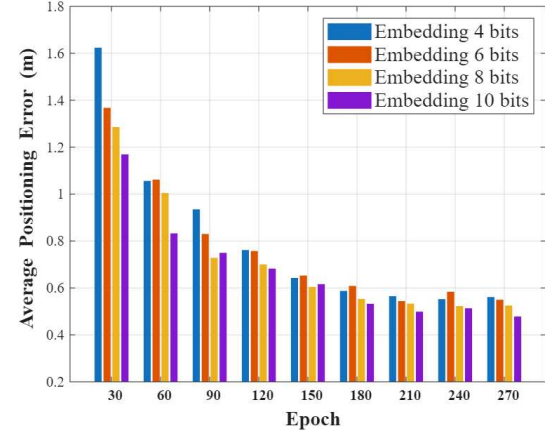


Fig. 8: Stage II validation mean error \bar{e} during training for different quantization resolutions Q .

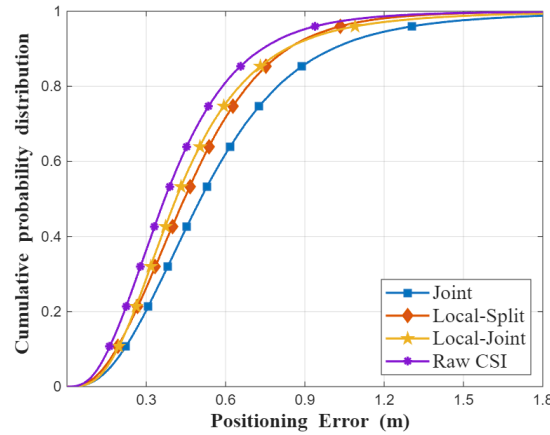


Fig. 9: CDF of the 3D localization error under $Q = 10$ for different training strategies.

Fig. 9 shows the CDF of the 3D localization error under $Q = 10$. Self-supervised local training consistently improves performance relative to training from scratch, indicating that Stage I provides a more stable and informative initialization. Moreover, Local Training–Joint Training outperforms Local Training–Split Training, confirming that propagating the localization loss through the quantization bottleneck better aligns the embedding with the downstream positioning task. At $Q = 10$, the proposed method approaches the lossless-CSI reference, suggesting that most positioning-relevant information is preserved in the quantized embedding.

Fig. 10 summarizes the accuracy–fronthaul trade-off across different Q . As Q decreases, quantization noise increases and the fidelity of phase-related cues (e.g., inter-antenna phase differences and multipath-induced frequency-dependent structures) can degrade, leading to larger localization errors. Across all tested bit depths, Local Training–Joint Training consistently achieves the best accuracy among the quantized schemes, especially in the low-bit regime.

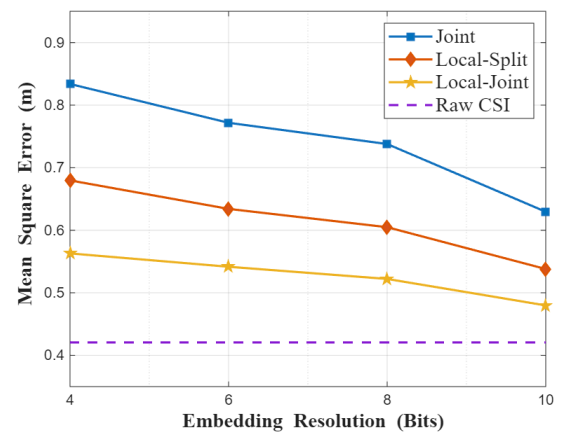


Fig. 10: Localization accuracy versus quantization resolution Q under different training strategies.

E. Comparison With Representative Baselines

We compare ECCNet with representative model-based and learning-based baselines:

- **ECCNet**: the proposed multi-BS cooperative ECC architecture with $Q = 10$ (cf. Fig. 2).
- **Transformer**: an ablation that replaces channel-masked attention (CMA) with standard multi-head self-attention across BS tokens (i.e., without gain-based masking), following [51].
- **ADCPM**: a cooperative fingerprinting baseline using ADCPM features as in [38] with a SegNet–MLP backbone.
- **MFCNet**: a deep-learning-based positioning baseline designed for OFDM systems [52].
- **MUSIC**: an AoA-based pipeline that estimates angles using MUSIC and then performs geometric triangulation.

Fair comparison protocol: All learning-based baselines are trained and evaluated under the same simulator distribution and with the same on-the-fly sample generation protocol. For each method, we explicitly follow its required input representation at the CU (losslessly forwarded CSI / BS-side

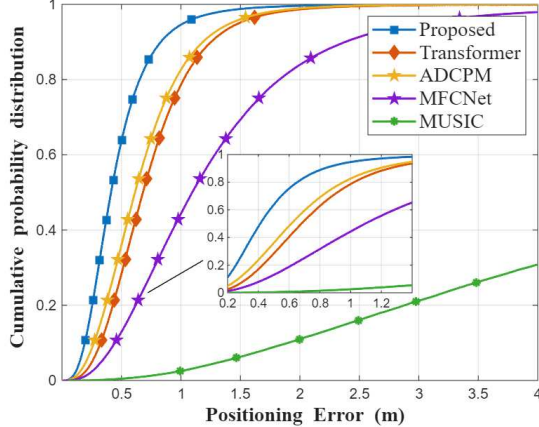


Fig. 11: CDF of the 3D localization error for different positioning methods.

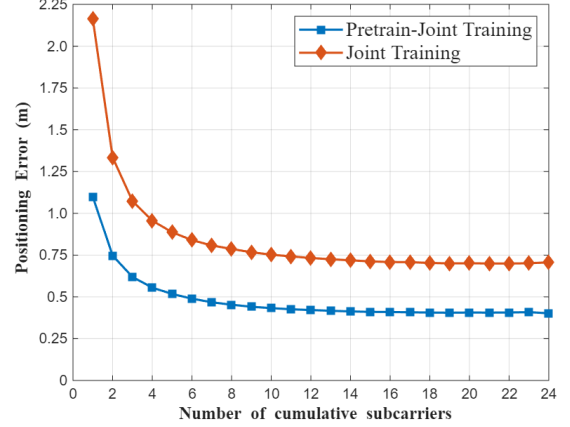


Fig. 12: Effect of accumulating frequency-domain features on localization accuracy.

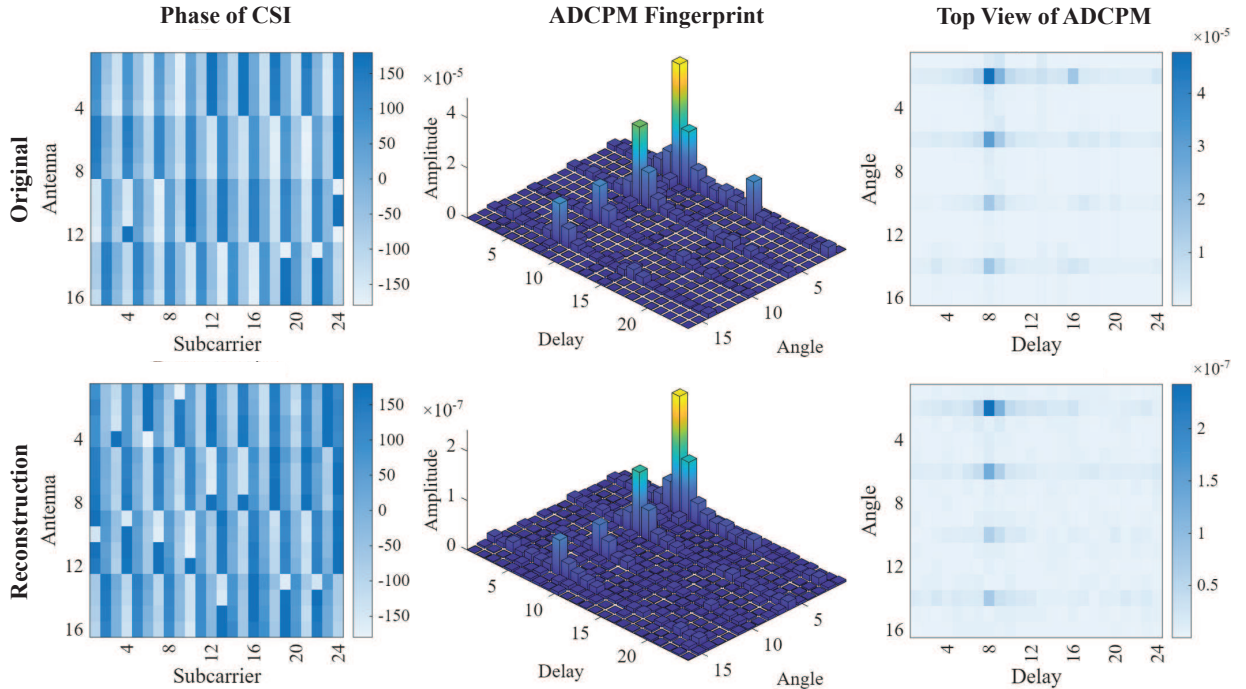


Fig. 13: Visualization of original and reconstructed CSI performed by distributed BS. Left: Phase of original CSI and reconstruction. Middle: ADCPM fingerprint of original CSI and reconstruction. Right: top view of ADCPM fingerprint and reconstruction.

engineered features / quantized embeddings), and we report fronthaul ratios separately when the input representations imply different fronthaul budgets.

Fig. 11 reports the CDF of the 3D localization error. The AoA-only MUSIC pipeline performs poorly in this urban setting, which is consistent with NLOS-dominated propagation where dominant components may correspond to reflections rather than a direct path. In contrast, ECCNet learns a task-oriented mapping from wideband multi-antenna multipath signatures to 3D location and achieves the best overall accuracy under the considered fronthaul constraint.

F. Benefit of Frequency Evidence Accumulation

Fig. 12 evaluates the effect of accumulating frequency-domain evidence in the proposed sequence model. As more subcarriers are included, the localization error decreases rapidly and then saturates.

This behavior is consistent with two properties of wideband OFDM channels. First, using more subcarriers increases the effective bandwidth and provides richer frequency-dependent multipath structure, improving delay-related discrimination. Second, frequency-selective fading may create deep nulls on individual subcarriers; aggregating across subcarriers reduces sensitivity to unreliable frequencies and improves robustness.

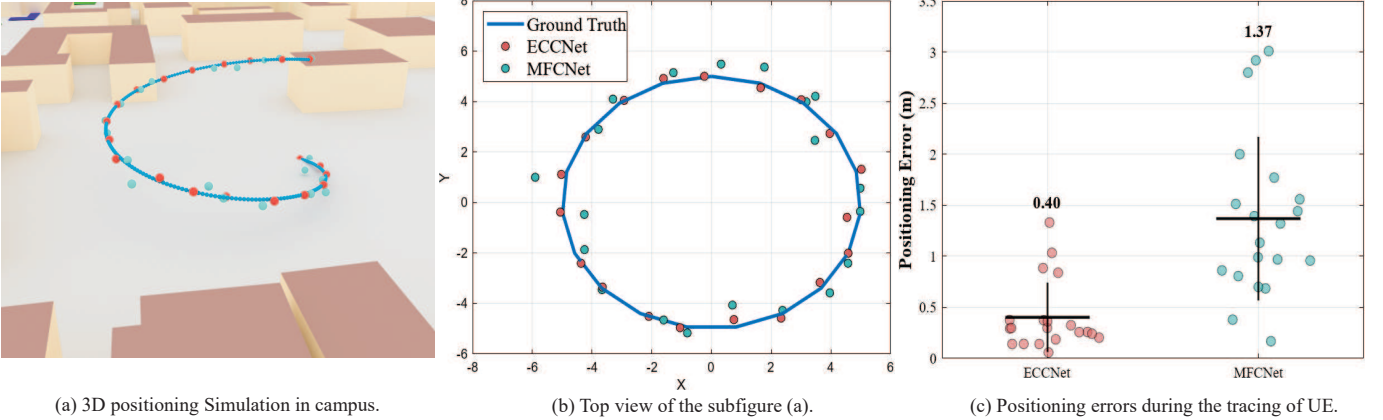


Fig. 14: 3D trajectory tracking simulation. Left: ground-truth and predicted trajectories from ECCNet ($Q = 10$) and MFCNet. Middle: Euclidean localization error along the trajectory. Right: top view.

G. Qualitative Visualization and Trajectory Tracking

1) Reconstruction behavior during Stage I local training:

To visualize what the embedding network preserves during self-supervised initialization, The left column of Fig. 13 compares representative phase responses derived from the original CSI and the Res-SegNet reconstruction during Stage I. The reconstructed phase patterns closely match the originals, indicating that salient phase structure across antennas and subcarriers is preserved by the embedding network.

Since the cosine-similarity objective in (22) is invariant to global scaling, it does not directly enforce amplitude matching. To further visualize multipath-related structure, we compare ADCPM fingerprints computed from the original and reconstructed CSI [38]. The dominant peak structures are preserved qualitatively, although the overall amplitude scale may differ.

2) 3D trajectory tracking: We further evaluate the tracking capability of ECCNet in the same ray-tracing environment using a continuous UE trajectory. The CSI corresponding to each trajectory point is fed into the trained models. We compare ECCNet with $Q = 10$ against MFCNet [52] as a representative learning-based baseline.

The UE follows a smooth 3D spiral trajectory: the horizontal path completes three revolutions with an approximate radius of 6 m, while the altitude increases from 0 m to 30 m. Fig. 14 shows that ECCNet tracks the ground-truth trajectory more closely in both horizontal and vertical dimensions. The mean Euclidean tracking error along the trajectory is approximately 0.40 m for ECCNet and 1.37 m for MFCNet.

V. CONCLUSIONS

In this paper, we developed a fronthaul-efficient edge–cloud cooperative (ECC) framework for distributed 3D positioning using wideband multi-antenna CSI. For distributed BSs, we designed a lightweight residual SegNet encoder to compress and embed the estimated CSI for fronthaul transmission under an explicit bit budget. At the cloud unit, 3D coordinates are inferred *directly* from the received embeddings by combining channel-masked attention with an LSTM-based frequency evidence accumulation network. Furthermore, we proposed a two-stage training pipeline to stabilize learning under quantization

constraints. Simulations in a 3.5 GHz 5G NR-compliant urban ray-tracing scenario with six BSs and 20 MHz bandwidth demonstrate sub-meter 3D positioning accuracy while substantially reducing fronthaul payload. Overall, the results validate the feasibility and effectiveness of task-oriented *embedding-for-positioning* fronthaul interfaces for scalable cooperative localization.

REFERENCES

- [1] A. Liu et al., “A Survey on Fundamental Limits of Integrated Sensing and Communication,” *IEEE Communications Surveys & Tutorials*, vol. 24, no. 2, pp. 994-1034, 2022.
- [2] Y. Yang et al., “Positioning Using Wireless Networks: Applications, Recent Progress, and Future Challenges,” *IEEE Journal on Selected Areas in Communications*, vol. 42, no. 9, pp. 2149-2178, 2024.
- [3] Ivanov, V., Volkov, A. and Peters, D. R. “Geometrical modeling and experimental measurements of indoor mmWave communication systems including finite-area reflective surfaces,” *Progress In Electromagnetics Research*, vol. 182, pp. 107-119, 2025.
- [4] J. Zhao, J. Chen, B. Cheng, B. Qian, Y. Xu and H. Zhou, “Cost-Effective Deployment for Fully-Decoupled RAN: A Techno-Economic Approach,” *IEEE Transactions on Vehicular Technology*, vol. 73, no. 11, pp. 17007-17023, 2024.
- [5] B. Fan, H. Tian, L. Jiang and A. V. Vasilakos, “A Social-Aware Virtual MAC Protocol for Energy-Efficient D2D Communications Underlying Heterogeneous Cellular Networks,” *IEEE Transactions on Vehicular Technology*, vol. 67, no. 9, pp. 8372-8385, 2018.
- [6] Q. Yu et al., “A Fully-Decoupled RAN Architecture for 6G Inspired by Neurotransmission,” *Journal of Communications and Information Networks*, vol. 4, no. 4, pp. 15-23, Dec. 2019.
- [7] J. Zhao, Q. Yu, B. Qian, K. Yu, Y. Xu, H. Zhou, “Fully-decoupled radio access networks: A resilient uplink base stations cooperative reception framework,” *IEEE Transactions on Wireless Communications*, vol. 22, no. 8, pp. 5096-5110, 2023.
- [8] Q. Peng, H. Ren, C. Pan, N. Liu and M. Elkashlan, “Resource Allocation for Uplink Cell-Free Massive MIMO Enabled URLLC in a Smart Factory,” *IEEE Transactions on Communications*, vol. 71, no. 1, pp. 553-568, 2023.
- [9] Q. Peng, H. Ren, M. Dong, M. Elkashlan, K. -K. Wong and L. Hanzo, “Resource Allocation for Cell-Free Massive MIMO-Aided URLLC Systems Relying on Pilot Sharing,” *IEEE Journal on Selected Areas in Communications*, vol. 41, no. 7, pp. 2193-2207, 2023.
- [10] R. K. Martin, C. Yan, H. H. Fan and C. Rondeau, “Algorithms and Bounds for Distributed TDOA-Based Positioning Using OFDM Signals,” *IEEE Transactions on Signal Processing*, vol. 59, no. 3, pp. 1255-1268, 2011.
- [11] R. Schmidt, “Multiple emitter location and signal parameter estimation,” *IEEE Transactions on Antennas and Propagation*, vol. 34, no. 3, pp. 276-280, 1986.

[12] A. Ramírez-Arroyo, A. Alex-Amor, P. Padilla and J. F. Valenzuela-Valdés, "Joint Direction-of-Arrival and Time-of-Arrival Estimation With Ultra-Wideband Elliptical Arrays," *IEEE Transactions on Wireless Communications*, vol. 22, no. 12, pp. 9187-9200, 2023.

[13] H. C. So and L. Lin, "Linear Least Squares Approach for Accurate Received Signal Strength Based Source Localization," *IEEE Transactions on Signal Processing*, vol. 59, no. 8, pp. 4035-4040, 2011.

[14] Z. Li and T. Braun, "Passively Track WiFi Users With an Enhanced Particle Filter Using Power-Based Ranging," *IEEE Transactions on Wireless Communications*, vol. 16, no. 11, pp. 7305-7318, 2017.

[15] S. Tomic, M. Beko and R. Dinis, "3-D Target Localization in Wireless Sensor Networks Using RSS and AoA Measurements," *IEEE Transactions on Vehicular Technology*, vol. 66, no. 4, pp. 3197-3210, 2017.

[16] Jia-Jia Jiang, Fa-Jie Duan, and Jin Chen, "Three-Dimensional Localization Algorithm for Mixed Near-Field and Far-Field Sources Based on ESPRIT and MUSIC Method," *Progress In Electromagnetics Research*, vol. 136, pp. 435-456, 2013.

[17] Peng Yang, Feng Yang, and Zai-Ping Nie, "DOA Estimation with Sub-Array Divided Technique and Interpolated ESPRIT Algorithm on a Cylindrical Conformal Array Antenna," *Progress In Electromagnetics Research*, vol. 103, pp. 201-216, 2010.

[18] S. D. Bast, A. P. Guevara and S. Pollin, "CSI-based Positioning in Massive MIMO systems using Convolutional Neural Networks," *2020 IEEE 91st Vehicular Technology Conference (VTC2020-Spring)*, Antwerp, Belgium, pp. 1-5, 2020.

[19] X. Wang, L. Gao and S. Mao, "CSI Phase Fingerprinting for Indoor Localization With a Deep Learning Approach," *IEEE Internet of Things Journal*, vol. 3, no. 6, pp. 1113-1123, 2016.

[20] B. Zhang, H. Sifaou and G. Y. Li, "CSI-Fingerprinting Indoor Localization via Attention-Augmented Residual Convolutional Neural Network," *IEEE Transactions on Wireless Communications*, vol. 22, no. 8, pp. 5583-5597, 2023.

[21] Weijian Si, Liangtian Wan, Lutao Liu, and Zuoxi Tian, "Fast Estimation of Frequency and 2-d DOAs for Cylindrical Conformal Array Antenna Using State-Space and Propagator Method," *Progress In Electromagnetics Research*, vol. 137, pp. 51-71, 2013.

[22] X. Xie, C. Hua, J. Hong and W. Xu, "Optimal Power Control and CSI Acquisition for Over-the-Air Computation in OFDM System," *IEEE Transactions on Wireless Communications*, vol. 23, no. 6, pp. 6533-6545, 2024.

[23] W. Ding, F. Yang, S. Liu, X. Wang and J. Song, "Nonorthogonal Time-Frequency Training-Sequence-Based CSI Acquisition for MIMO Systems," *IEEE Transactions on Vehicular Technology*, vol. 65, no. 7, pp. 5714-5719, 2016.

[24] J. Tang et al., "Massive MIMO-OFDM Channel Acquisition With Time-Frequency Phase-Shifted Pilots," *IEEE Transactions on Communications*, vol. 73, no. 6, pp. 4520-4535, 2025.

[25] S. Shi, S. Sigg, L. Chen and Y. Ji, "Accurate Location Tracking From CSI-Based Passive Device-Free Probabilistic Fingerprinting," *IEEE Transactions on Vehicular Technology*, vol. 67, no. 6, pp. 5217-5230, 2018.

[26] Marija Agatonovic, Zoran Stankovic, Ivan Milovanovic, Nebojsa Doncov, Leen Sit, Thomas Zwick, and Bratislav Milovanovic, "Efficient Neural Network Approach for 2D DOA Estimation Based on Antenna Array Measurements," *Progress In Electromagnetics Research*, vol. 137, pp. 741-758, 2013.

[27] B. Camajori Tedeschini, M. Brambilla, L. Barbieri, G. Balducci and M. Nicoli, "Cooperative Lidar Sensing for Pedestrian Detection: Data Association Based on Message Passing Neural Networks," *IEEE Transactions on Signal Processing*, vol. 71, pp. 3028-3042, 2023.

[28] Quanfeng Wang, Alexander H. Paulus, Mei Song Tong, and Thomas F. Eibert, "An Indoor Localization Technique Utilizing Passive Tags and 3-D Microwave Passive Radar Imaging," *Progress In Electromagnetics Research*, vol. 181, pp. 89-98, 2024.

[29] J. Du, J. Cao, L. Jin, S. Li, J. Liu and F. Gao, "Indoor Vehicle Positioning for MIMO-OFDM WIFI Systems via Rearranged Sparse Bayesian Learning," *IEEE Transactions on Wireless Communications*, vol. 23, no. 7, pp. 7849-7864, 2024.

[30] X. Cheng, D. Duan, S. Gao and L. Yang, "Integrated Sensing and Communications (ISAC) for Vehicular Communication Networks (VCN)," *IEEE Internet of Things Journal*, vol. 9, no. 23, pp. 23441-23451, 2022.

[31] Siyuan Shao, Min Fan, Cheng Yu, Yan Li, Xiaodong Xu, and Haiming Wang, "Machine Learning-Assisted Sensing Techniques for Integrated Communications and Sensing in WLANs: Current Status and Future Directions (Invited)," *Progress In Electromagnetics Research*, vol. 175, pp. 45-79, 2022.

[32] H. Zou, M. Jin, H. Jiang, L. Xie and C. J. Spanos, "WinIPS: WiFi-Based Non-Intrusive Indoor Positioning System With Online Radio Map Construction and Adaptation," *IEEE Transactions on Wireless Communications*, vol. 16, no. 12, pp. 8118-8130, 2017.

[33] K. Gao, H. Wang, H. Lv and W. Liu, "Toward 5G NR High-Precision Indoor Positioning via Channel Frequency Response: A New Paradigm and Dataset Generation Method," *IEEE Journal on Selected Areas in Communications*, vol. 40, no. 7, pp. 2233-2247, 2022.

[34] E. Gönlütaş, E. Lei, J. Langerman, H. Huang and C. Studer, "CSI-Based Multi-Antenna and Multi-Point Indoor Positioning Using Probability Fusion," *IEEE Transactions on Wireless Communications*, vol. 21, no. 4, pp. 2162-2176, 2022.

[35] H. Park, S. Chung, J. Park, and Y. Huang, "High-Resolution Localization Using Distributed MIMO FMCW Radars," *Sensors*, vol. 25, no. 12, pp. 3579-3579, 2025.

[36] S. Wang, X. Jiang and H. Wymeersch, "Cooperative Localization in Wireless Sensor Networks With AOA Measurements," *IEEE Transactions on Wireless Communications*, vol. 21, no. 8, pp. 6760-6773, 2022.

[37] B. C. Tedeschini and M. Nicoli, "Cooperative Deep-Learning Positioning in mmWave 5G-Advanced Networks," *IEEE Journal on Selected Areas in Communications*, vol. 41, no. 12, pp. 3799-3815, 2023.

[38] C. Wu et al., "Learning to Localize: A 3D CNN Approach to User Positioning in Massive MIMO-OFDM Systems," *IEEE Transactions on Wireless Communications*, vol. 20, no. 7, pp. 4556-4570, 2021.

[39] J. Guo, C. -K. Wen, S. Jin and G. Y. Li, "Overview of Deep Learning-Based CSI Feedback in Massive MIMO Systems," *IEEE Transactions on Communications*, vol. 70, no. 12, pp. 8017-8045, 2022.

[40] C. -K. Wen, W. -T. Shih and S. Jin, "Deep Learning for Massive MIMO CSI Feedback," *IEEE Wireless Communications Letters*, vol. 7, no. 5, pp. 748-751, 2018.

[41] X. -L. Huang, J. Wu, Y. Wen, F. Hu, Y. Wang and T. Jiang, "Rate-Adaptive Feedback With Bayesian Compressive Sensing in Multiuser MIMO Beamforming Systems," *IEEE Transactions on Wireless Communications*, vol. 15, no. 7, pp. 4839-4851, 2016.

[42] P. Liang, J. Fan, W. Shen, Z. Qin and G. Y. Li, "Deep Learning and Compressive Sensing-Based CSI Feedback in FDD Massive MIMO Systems," *IEEE Transactions on Vehicular Technology*, vol. 69, no. 8, pp. 9217-9222, 2020.

[43] J. Guo, C. -K. Wen, S. Jin and G. Y. Li, "Convolutional Neural Network-Based Multiple-Rate Compressive Sensing for Massive MIMO CSI Feedback: Design, Simulation, and Analysis," *IEEE Transactions on Wireless Communications*, vol. 19, no. 4, pp. 2827-2840, 2020.

[44] G. Huang, A. Liu and M. -J. Zhao, "Two-Stage Adaptive and Compressed CSI Feedback for FDD Massive MIMO," *IEEE Transactions on Vehicular Technology*, vol. 70, no. 9, pp. 9602-9606, 2021.

[45] X. Liang, H. Chang, H. Li, X. Gu and L. Zhang, "Changeable Rate and Novel Quantization for CSI Feedback Based on Deep Learning," *IEEE Transactions on Wireless Communications*, vol. 21, no. 12, pp. 10100-10114, 2022.

[46] X. Zhang, Z. Lu, R. Zeng and J. Wang, "Quantization Adaptor for Bit-Level Deep Learning-Based Massive MIMO CSI Feedback," *IEEE Transactions on Vehicular Technology*, vol. 73, no. 4, pp. 5443-5453, 2024.

[47] Y. Ma, H. He, S. Song, J. Zhang and K. B. Letaief, "Low-Complexity CSI Feedback for FDD Massive MIMO Systems via Learning to Optimize," *IEEE Transactions on Wireless Communications*, vol. 24, no. 4, pp. 3483-3498, 2025.

[48] V. Badrinarayanan, A. Kendall and R. Cipolla, "SegNet: A Deep Convolutional Encoder-Decoder Architecture for Image Segmentation," *IEEE Transactions on Pattern Analysis and Machine Intelligence*, vol. 39, no. 12, pp. 2481-2495, 2017.

[49] J. Hoydis et al., "Sionna: An open-source library for next-generation physical layer research," Mar. 2022, arXiv:2203.11854.

[50] Unwiredlabs. OpenCellid. Accessed: Sep. 2024. [Online]. Available: <https://www.opencellid.org>.

[51] A. Vaswani et al., "Attention is all you need," *Neural Information Processing Systems*, pp. 5998-6008, Jun. 2017.

[52] Z. Chen, Z. Zhang, Z. Xiao, Z. Yang and R. Jin, "Deep Learning-Based Multi-User Positioning in Wireless FDMA Cellular Networks," *IEEE Journal on Selected Areas in Communications*, vol. 41, no. 12, pp. 3848-3862, 2023.